Citation for final published version:

Nasane, Mamta P., Rondiya, Sachin R., Jadhav, Chandradip D., Rahane, Ganesh, Cross, Russell William, Jathar, Sagar, Jadhav, Yogesh, Barma, Sunil, Nilegave, Dhanraj, Jadkar, Vijaya, Rokade, Avinash, Funde, Adinath M, Chavan, Padmakar G., Hoye, Robert L Z, Dzade, Nelson Yaw ORCID: https://orcid.org/0000-0001-7733-9473 and Jadkar, Sandesh R 2021. An interlinked computational-experimental investigation into SnS nano-flakes for field emission application. New Journal of Chemistry 45 , pp. 11768-11779. 10.1039/D1NJ00902H file

Publishers page: http://dx.doi.org/10.1039/D1NJ00902H <http://dx.doi.org/10.1039/D1NJ00902H>

An Interlinked Computational-Experimental Investigation into SnS Nano-Flakes for Field Emission Application

Mamta P. Nasane[1], Sachin R. Rondiya[2*], Chandradip Jadhav[3], Ganesh Rahane[1], Russell W. Cross[2], Sagar Jathar[1], Yogesh Jadhav[1], Sunil Barma[1], Dhanaraj Nilegave[1], Vijaya Jadkar[1], Avinash Rokade[1], Adinath Funde[1], Padmakar Chavan[4], Robert Hoye[5], Nelson Y. Dzade[2*], Sandesh Jadkar[6*]

[1]School of Energy Studies, Savitribai Phule Pune University, Pune 411 007 **(India)**

[2]School of Chemistry, Cardiff University, Main Building, Park Place, Cardiff, CF10 3AT, Wales, **(UK)**

[3]The State Key Laboratory of Refractories and Metallurgy, Institute of Advanced Materials and Nanotechnology, College of Materials and Metallurgy, Wuhan University of Science and Technology, Wuhan 430081 **(China)**

[4]Department of Physics, School of Physical Sciences, Kavayitri Bahinabai Chaudhari North Maharashtra University, Jalgaon 425001 **(India)**

[5]Department of Materials, Imperial College London, Exhibition Road, London SW7 2AZ, **(UK)**

[6]Department of Physics, Savitribai Phule Pune University, Pune 411 007 **(India)**

***Corresponding authors:**

E-mail: sandesh@physics.unipune.ac.in (Sandesh Jadkar), RondiyaS@cardiff.ac.uk (Sachin R. Rondiya), dzadeny@cardiff.ac.uk (Nelson Y. Dzade)

ABSTRACT

Layered binary semiconductor materials have attracted significant interest as field emitters due to their low work function, mechanical stability, high thermal and electrical conductivity. Herein, we report a systematic experimental and theoretical investigation of SnS nanoflakes synthesized using a simple, low-cost, and non-toxic hot injection method for field emission studies. The field emission studies were carried out on SnS nanoflakes thin film prepared using a simple spin coat technique. The x-ray diffraction (XRD) and Raman spectroscopy analysis revealed an orthorhombic phase of SnS. Scanning electron microscopy (SEM) analysis revealed that as-synthesized SnS has flakes-like morphology. The formation of pure-phase SnS nanoflakes was further confirmed by x-ray photoelectron spectroscopy (XPS) analysis. The UV-Visible-NIR spectroscopy analysis shows that SnS nanoflakes have a sharp absorption edge observed in the UV region and have a band gap of ~ 1.66 eV. In addition, the first-principles density functional theory

(DFT) calculations were carried out to provide atomic-level insights into the crystal structure, band structure, and density of states (DOS) of SnS nanoflakes. The field emission properties of SnS nanoflakes were also investigated and found that SnS nanoflakes have a low turn-on field (~ 6.2 V/μm for 10 μA/cm^2), high emission current density (~ 104 μA/cm^2 at 8.0 V/μm), superior current stability (~ 2.5 hrs for ~ 1 μA) and a high field enhancement factor of 1735. The first principle calculations the predicted lower work function of different surfaces, especially for the most stable SnS (001) surface (ϕ = 4.32 eV), is believed to be responsible for the observed facile electron emission characteristics. We anticipate that the SnS could be utilized for future vacuum nano/microelectronic and flat panel display applications due to the low turn-on field and flakes-like structure.

KEYWORDS: SnS, nano-structures, field emission, hot-injection method, density functional theory

1: INTRODUCTION

By definition, field electron emission is the extraction of electrons from metals or semiconductor materials via quantum tunneling through the surface potential barrier by applying a strong electric field, typically of the order of 10^6-10^7 V/cm [1]. A variety of nanomaterials such as carbon nanotubes (CNT) [2], graphene [3], molybdenum disulfide (MoS_2) [4], gallium sulfide (GaS) [5], tungsten disulfide (WS_2) [6], indium antimonide (InSb) [7], gallium selenide (GaSe) [8], niobium nitride (NbN) and niobium disulfide (NbS_2) [9], niobium diselenide ($NbSe_2$) [10], hexagonal boron nitride (h-BN) [11], zinc oxide (ZnO) [12], black phosphorous (BP) [13], titanium trisulfide (TiS_3) [14], reduced graphene oxide (rGO) [15], tin monosulphide (SnS) [16], silicon carbide (SiC) [17], lanthanum hexaboride (LaB_6) [18], cerium hexaboride (CeB_6) [19], klockmannite (CuSe) [20] etc. has been synthesized and explored for field emission application. These materials have demonstrated numerous applications in telecommunication satellites, medical devices, space research, x-ray sources, and electronic displays. Among these, SnS has demonstrated strong potential as a field emitter due to its low turn-on field, high emission current density, and superior current stability [21]. Moreover, it is a simple binary system that contains non-toxic, inexpensive, and relatively earth-abundant elements. It is a p-type semiconductor compound having a layered orthorhombic crystal structure having indirect (1 to 1.5 eV) and direct band gap (1.39 to 2.33 eV) depending upon the preparation method and heat treatment temperature [22]. Due to inimitable properties, SnS has been successfully employed in various applications, including opto-electronics [23], heterojunction thin-film solar cells [24], semiconductor-sensitized solar cells [25], lithium-ion batteries [26], near-infra-red detectors [27], photocatalysts [28], sensors [29], solid-state lubricants [30], supercapacitors [31], micro-batteries [32] and photoluminescence [33] etc.

Various deposition techniques have been used for the synthesis of SnS thin films, including vapor-phase transport [34], electrochemical deposition [35], electron beam evaporation [36], chemical bath deposition (CBD) [37], thermal evaporation technique [38], plasma-enhanced chemical vapor deposition (PE-CVD) [39], hydrothermal method [40], chemical spray pyrolysis [41], liquid-phase deposition [42], aerosol assisted CVD [43], successive ionic layer adsorption and reaction (SILAR) [44], microwave-assisted solvothermal [45], and hot injection method (HIM) [46], etc. Each method has its advantages and limitations. Although these methods synthesize SnS thin films, almost all these synthesis methods require toxic reagents/surfactants, longer reaction times at relatively high temperatures, or special artificial reaction conditions such as a high vacuum environment. The requirement of special reaction conditions for the synthesis of SnS limits the practical applications. Therefore, the synthesis of SnS by using an environmentally stable precursor under simple reaction conditions is necessary. The HIM is a facile, low-cost, and robust solution-phase colloidal synthesis route that offers excellent phase control of nanomaterials by optimizing the reaction temperature, precursor molar ratios and solvent types, etc. The HIM method is also suitable for the large-scale synthesis of SnS films. Furthermore, synthesis conditions in HIM such as reaction time, reaction temperature, and concentration of the organic ligands are easily controlled to achieve well crystalline, mono-disperse nanoparticles having different shapes and sizes.

Up to now, SnS nanocrystals have been reported by using the hot-injection method for various applications. For example, *Koktysh et al.* [47] synthesized size-controlled SnS nanocrystals in oleylamine using the HIM from tin(II) chloride and dimethylammonium diethyldithiocarbamate in the presence of dodecanethiol for photoelectronic device applications. *Wu* and others [46] reported the synthesis of SnS nanoparticles by using the hot-injection method photoelectrochemical (PEC) water splitting. Phase pure SnS nanosheets were synthesized by *Khan et al.* [48] using a hot-injection method from a single molecular precursor (SMP), dibutyl-bis(piperidinedithiocarbamato)tin(IV) in oleylamine at 230 °C. *Huang* and co-workers [49] obtained orthorhombic and metastable phase SnS nanocrystals using the hot-injection method to investigate the photoelectrochemical activity. To the best of our knowledge, the synthesis of

SnS nanoflakes using the hot-injection method for field emission application has not been reported, and no report exists in the literature. With this motivation, an attempt has been made to prepare SnS nanoflakes by using the hot-injection method. The formation of single-phase SnS has been confirmed by x-ray diffraction and Raman spectroscopy. The formation of nanoflakes was confirmed by scanning electron microscopy (SEM). The field emission (FE) studies of the as-synthesized SnS nanoflakes have also been carried out. Finally, the density functional theory (DFT) calculations have been performed to obtain atomic-level insights about the surface structure, optical (band gap), and electrical properties (work function) of the SnS nanoflakes. The obtained results demonstrate the potential of SnS nanoflakes emitter as an electron source for practical applications in vacuum nano/microelectronic devices.

2: EXPERIMENTAL

2.1: Materials and Chemicals

Tin chloride ($SnCl_2 \cdot 2H_2O$, ≥ 99 %), oleylamine (OAm, ≥ 99 %), octadecane (ODE, ≥ 99 %), oleic acid (OA, ≥ 99 %), sulphur powder (S, ≥ 99 %), isopropanol (IPA, ≥ 99.5 %), toluene (≥ 99.8 %) were purchased from Sigma Aldrich and used as-received.

2.2: Synthesis of SnS nanoflakes

The SnS nanoflakes were synthesized via the hot injection method as per the protocol reported previously [50, 51] with some minor modifications. The synthesis was carried out in three different steps viz. first, preparation of tin (Sn) precursor, second preparation of sulphur (S) precursor, and finally the injection of S precursor into Sn precursor at nucleation temperature. In detail, for the synthesis of SnS nano-flakes, freshly weighed 1 mmol (0.2256 g) of tin chloride ($SnCl_2 \cdot 2H_2O$) was dissolved in 10 ml of ODE with 2 ml of OLA and 1 ml of OA in a 100 mL three-necked flask with continuous magnetic stirring at 600 rpm. This solution is heated to 120 °C in an Ar environment with constant stirring, followed by degassing for 10 min to remove water and air from the flask. Once the degassing is completed, the solution was further heated to 280 °C for 10 min to obtain a clear and transparent solution. It indicates the formation of the Sn-oleate complex. Simultaneously, the S precursor (S-OLA) was prepared by dissolving 1.85 mmol (0.0593 g) of sulphur powder in 5 ml of OLA with magnetic stirring at 600 rpm under Ar flow. The 5 mL S-OLA solution was swiftly injected into the Sn-oleate complex at nucleation temperature 280 °C. The immediate change in color from clear to brown was noticed, indicating the SnS nucleation process. The temperature was maintained at 280 °C for 15 min for further growth of SnS nanoflakes. After the completion of the reaction, the solution was allowed to cool naturally. The SnS nano-flakes separated from the mother liquor by precipitation using 4 ml toluene and 40 ml IPA solution followed by centrifugation for 15 min at 5000 rpm. The washing process was repeated three times to remove all remaining organic solvents, surfactants, and unreacted precursors. The solid SnS nanoflakes were collected after centrifugal drying under an IR lamp and used for further characterization. The thin films were prepared using 2 mg of SnS powder dispersed in 0.1 ml of toluene. This dispersion was coated on a pre-cleaned soda-lime glass substrate by spin coating techniques at 1500 rpm for 15 s and repeated twice. Figure 1 shows a schematic of the synthesis of SnS powder and thin films, which involved both hot injection (HI) and spin coating methods.

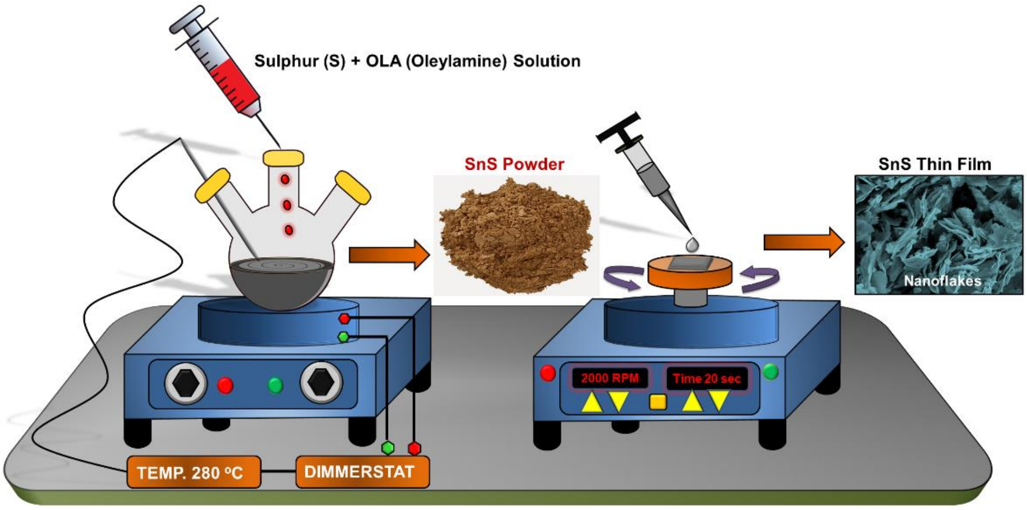

Figure 1: Schematic of SnS powder and thin films synthesis, involving hot injection and spin coating methods.

2.3: Material characterization

Various complementary analysis methods were used to characterized as-prepared SnS thin films. The X-ray diffraction pattern of prepared SnS samples was obtained using an x-ray diffractometer (Bruker D8 Advance, Germany) using CuKα line (λ = 1.54056 Å) in the diffraction angle range 2θ = 20-60°. Raman spectra were obtained in the range 50-350 cm^{-1} using a Raman spectrophotometer (Horibra-Jobin Yvon LABRAM-HR) with an excitation source of 532.8 nm laser. The spectrometer has backscattering geometry for the detection of Raman spectrum with the resolution of 1 cm^{-1}. The power of the Raman laser and its spot size were kept > 5 mW and ~ 1 μm, respectively, to avoid possible heating effects on the sample. The optical band gap and absorbance of SnS were deduced from the transmission data obtained using a JASCO, V-670, Japan UV-Visible spectrophotometer in the spectral range of 200-1200 nm. The x-ray photoelectron spectroscopy (XPS) characterization was carried out using a Kratos Axis DLD photoelectron spectrometer, utilizing monochromatic AlK_{α} radiation operating at an energy of 120 W. Scanning electron microscope (SEM) (FEG-SEM Model: Tescan Maia3) with an operating voltage of 5 kV was used to examine the morphology and surface topography of the SnS film. The energy dispersive

x-ray spectroscopy (EDX) was used for compositional analysis.

2.4: Field emission characterization

The field emission current density-applied field (J-E) and current-time (I-t) measurements were carried out by field emission microscope in a close proximity (planar diode) configuration. Figure 2 shows the schematic of the field emission geometrical setup used in the present study. The SnS nanoflakes deposited on soda-lime glass substrate served as cathode and a semitransparent cathodoluminescent phosphor screen as an anode. Provision of back contact was made using conducting carbon tape. The sample area was 1 $cm^{2,}$ and the separation between anode and cathode was 1 mm. The working chamber was evacuated using an ultrahigh vacuum system comprising of rotary backed turbo-molecular pump, sputter ion pump, and titanium sublimation pump. The cathode (SnS nano-flakes) did not show any appreciable degassing, and vacuum was obtained with the usual speed.

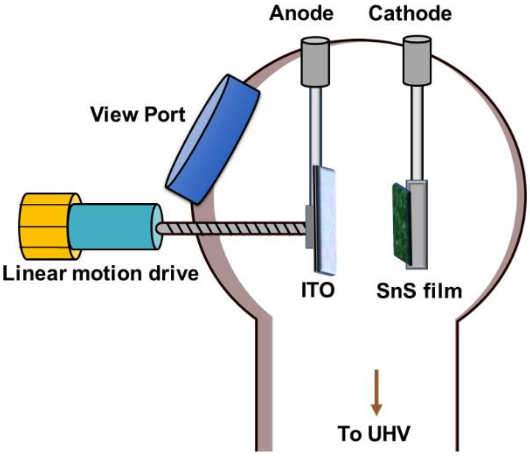

Figure 2: Schematic diagram of field emission setup geometry

After baking the system at 150 °C for 8 hrs, a base pressure of ~ 10^{-8} mbar was obtained. The J-E measurement was carried out at this base pressure using a Keithley 485 Picoammeter and a Spellman, USA high voltage DC power supply. Special care was taken to avoid any leakage current by using shielded cables with proper grounding.

2.5: Computational methods

First-principles DFT calculations were performed using the projector augmented wave (PAW) method [52], implemented in the Vienna ab-initio simulation package (VASP) [53]. Geometry optimizations applied the generalized gradient approximation (GGA), along with the Perdew-Burke-Ernzerhof (PBE) functional for the exchange-correlation potential [54]. The hybrid HSE-06 functional with 20 % Hartree-Fock screening was used for accurate electronic structure calculations [55]. A high plane-wave energy cut-off parameter was used of 600 eV, along with a convergence criterion of 10^{-6} eV between self-consistent steps and a Hellmann-Feynman force convergence value of 0.003 eV/Å. A Monkhorst-Pack k-point mesh of 9x9x3 was utilized for the bulk material [56]. The projected density of states (PDOS) and band structure was calculated using the tetrahedron method with Blöchl corrections [57].

The (111), (010), and (001) surfaces used to characterize the work function of SnS were created from the fully relaxed bulk SnS structure using the METADISE code, ensuring a zero-dipole perpendicular to the surface plane and no dangling bonds [58, 59]. A slab thickness of at least 15 Å was ensured with a vacuum region of 20 Å added to eliminate any interaction between adjacent layers in the z-direction. Surface energy (γ), which characterizes the stabilities of each surface, was calculated using

$$\gamma = \frac{E_{surface} - n\, E_{bulk}}{2\,A} \qquad \text{..... (1)}$$

Where $E_{surface}$ is the energy of the slab, E_{bulk} is the energy of the bulk unit cell, n is the number of bulk units in the SnS surface slab, and A is the surface area. A k-point mesh of 9x3x1 was used to model the SnS (111) and (010) surfaces, and 9x9x1 for (001). The surface work function (ϕ) was determined from the relation,

$$\phi = E_{vac} - E_F \qquad \text{..... (2)}$$

Where E_{vac} is the vacuum level and E_F is the Fermi level. A dipole correction perpendicular to each surface has been included within the VASP calculations to remove any net dipole, which may affect E_{vac} [60, 61].

3: RESULTS AND DISCUSSION

3.1: Structural properties

Structural properties and phase identification of SnS films were carried using x-ray diffraction (XRD). The XRD pattern of as-synthesized SnS film is shown in figure 3(a). The presence of multiple peaks in the diffraction pattern indicates the polycrystalline nature of SnS film. As seen, major diffraction peaks are observed at $2\theta \sim 22.62^\circ$, 26.63°, 28.04°, 31.04°, 32.14°, 32.55°, 39.66°, 43.17°, 45.67°, 49.18°, 51.88°, 53.99°, 54.79°, and 57.20° which are associated with (110), (120), (021), (101), (111), (040), (131) (141), (002), (211), (151), (112), (231), and (042), respectively. These peaks match the standard JCPDS data card # 39-0354, indicating the formation of the orthorhombic SnS phase (P_{bnm}-Space group 62) with lattice parameters a = 0.322 nm, b = 1.115 nm, and c = 0.601 nm [62]. These diffraction planes are consistent with those previously reported diffraction planes of orthorhombic SnS films [48, 63]. The dominant peak is at 2θ ~ 32.55° suggesting SnS crystallites have preferred orientation along (040) direction. No other impurity phases were observed in the XRD pattern indicating the formation of pure SnS film.

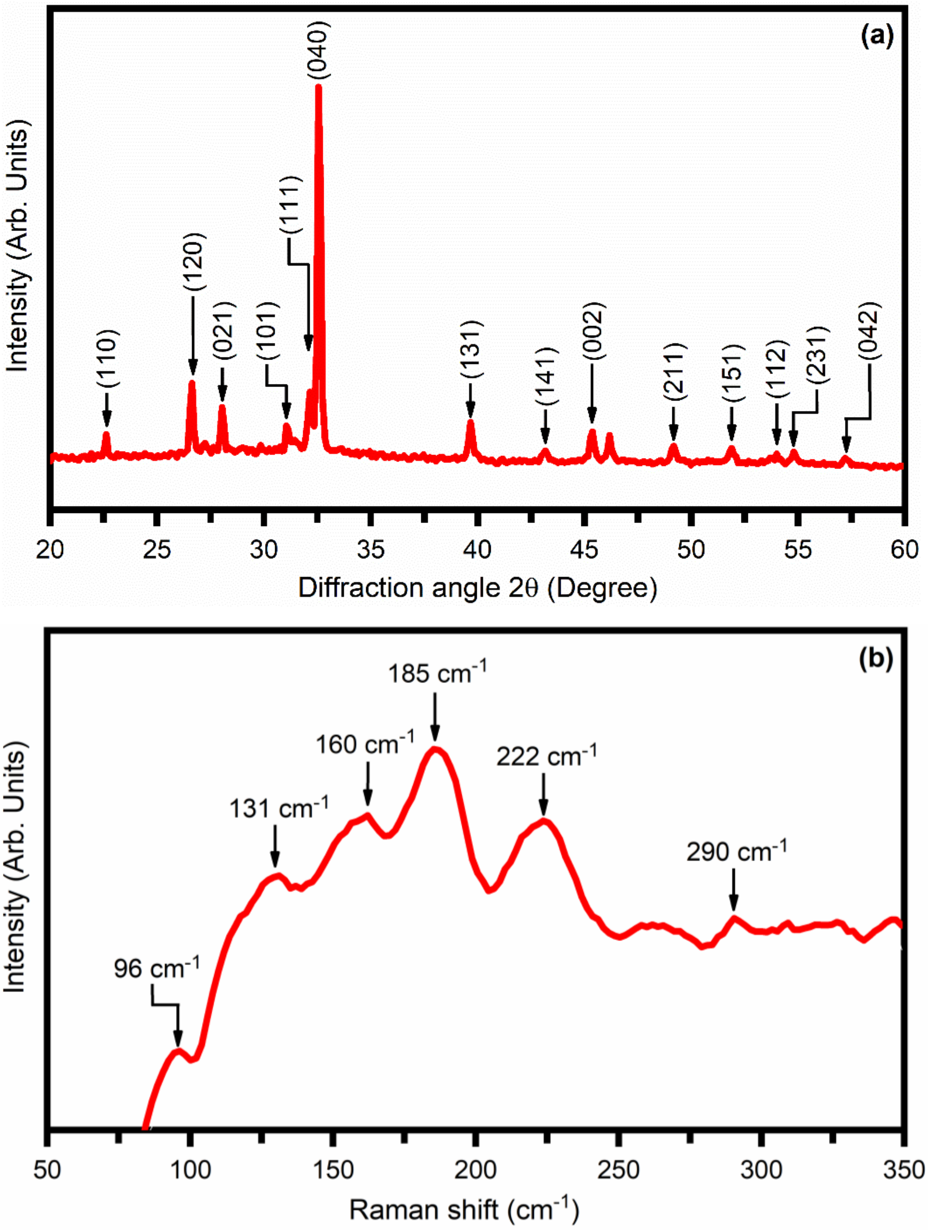

Figure 3: a) X-ray diffraction pattern and **b)** Raman spectra of the as-synthesized SnS thin film.

Applying the *Debye-Scherrer* formula, we have calculated the average crystallite size ($d_{x\text{-}ray}$) for the SnS film [64],

$$d_{x-ray} = \frac{0.9\ \lambda}{\beta \cos \theta_B} \qquad \text{..... (3)}$$

Where, λ is the wavelength of diffracted radiation (CuK$_\alpha$, λ = 1.54 Å), θ_B is the Bragg angle, and β is the full width at half maximum (FWHM) in radians indexed to the (040) plane. The calculated value of average crystallite size for SnS film is found ~ 42 nm.

The interplanar spacing (d_{040}) of the SnS nanoparticles is estimated using Bragg's equation,

$$d_{040} = \frac{n\,\lambda}{2\sin(\theta_B)} \qquad \ldots\ldots (4)$$

The calculated d_{040} value of SnS films (~ 2.798 Å) matches the previously reported value [65], which confirms the orthorhombic SnS phase formation.

Raman spectroscopy is a robust characterization method used to detect various material phases based on discrete vibrational modes representing the nature of the chemical bond and order of the atomic arrangement. SnS has 21 optical active modes, of which 12 are Raman active modes, 7 are infra-red active modes, and 2 are inactive. According to the reported literature A_g, B_{2g}, and B_{3g} are Raman active modes. At the same time, B_{2u} is the infra-red active mode of the SnS nano-structure [66]. Figure 3(b) shows the Raman spectrum of the SnS thin film. As can be seen in Figure 3(b), the Raman spectrum exhibits peaks at ~ 96 cm^{-1}, 131 cm^{-1}, 162 cm^{-1}, 185 cm^{-1}, and 222 cm^{-1} and 290 cm^{-1}, relating to different optical phonon modes of SnS. The peak at ~ 96 cm^{-1} corresponds to A_g mode, whereas the peak at ~ 141 cm^{-1} associated with B_{2u} mode and at ~ 160 cm^{-1} to B_{3g} mode. The peaks at ~ 185 cm^{-1} and at ~ 222 cm^{-1} are assigned to the longitudinal optical A_g (LO) modes. The peak at ~ 290 cm^{-1} corresponds to B_{2g} mode of SnS at room temperature. These results are consistent with the previously reported Raman spectra analysis of the orthorhombic SnS phase [67]. No Raman modes corresponding to impurity phases such as SnS_2, Sn_2S, and SnO_2 were found, demonstrating phase-purity of the SnS samples. These results are analogous to low angle XRD analysis.

3.2: Surface morphology and composition properties

The surface morphology of the as-prepared SnS film was examined using scanning electron microscopy (SEM). Figure 4(a) represents the SEM image of SnS film recorded at x25 K magnification. The image shows the formation of randomly distributed flake-like SnS nano-structures with an average size in the range of 600-2700 nm. Before imaging, the samples were coated with platinum by the sputtering method. Figure 4(a) shows the SnS flakes are dense, homogeneous, and free from flaws and cracks. These flakes act as potential emission sites in field emission due to enhancement in the local field.

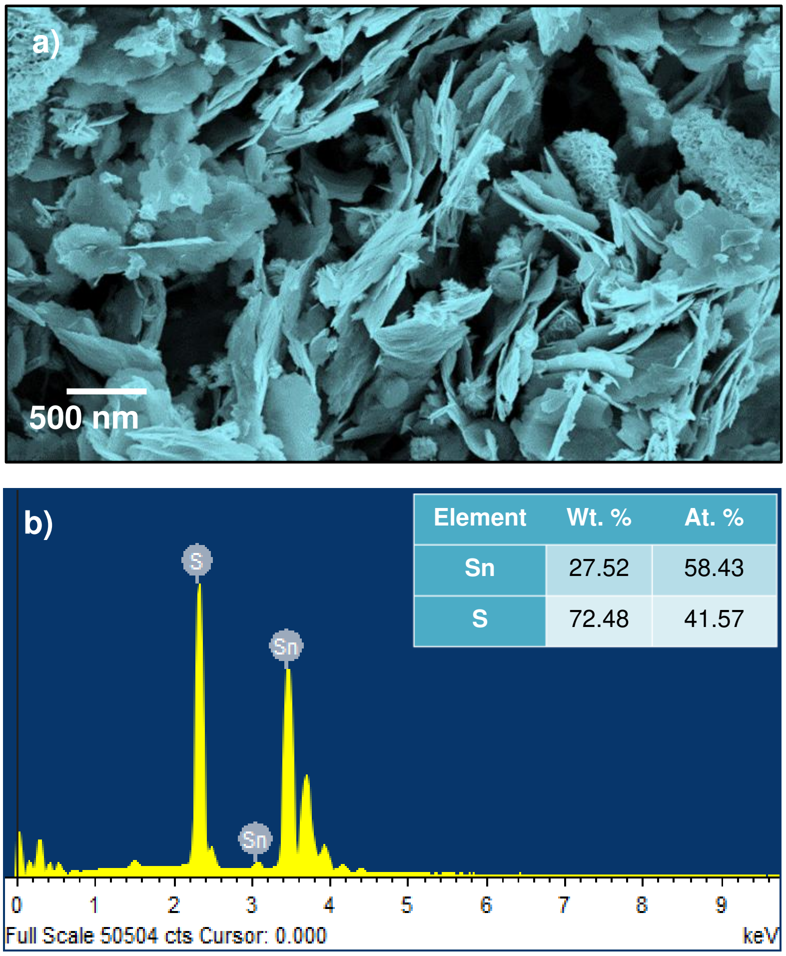

Element	Wt. %	At. %
Sn	27.52	58.43
S	72.48	41.57

Figure 4: a) SEM images of the SnS nano-structure **b)** The EDS spectra and the elemental mapping suggest even distribution of chemical constituents in the SnS nano-structure.

The chemical composition of SnS film was studied using energy-dispersive x-ray spectroscopy (EDAX). Figure 4(b) shows the EDAX spectrum of the SnS nano-flakes film. The inset shows the elemental mapping of Sn and S in the films. As seen, the ratio S/Sn is ~ 1 suggesting the stoichiometric formation of SnS film.

3.3: X-ray photoelectron spectroscopy (XPS) analysis

To determine the oxidation state of the as-prepared SnS nanoflakes, we have performed XPS measurements. Figure 5(a) shows the XPS survey scan (0-1000 eV) of SnS film. The XPS data were analyzed after the alignment to the C 1s peak as a reference. The binding energy was corrected for specimen charging through referencing the C 1s to 286 eV. The scan shows the presence of elemental tin (Sn), sulphur (S), oxygen (O), and carbon (C). The core-level peaks corresponding to the elements Sn and S can be visibly seen in the spectra. It also shows a C peak at ~ 286 eV and an O peak at ~ 532 eV as impurities. High-resolution measurements of the Sn-3d core peaks [Figure 5(b)] reveal a doublet spin-orbit peak at ~ 489.67 eV and ~ 498.18 eV, which are assigned to Sn^{2+} $3d_{5/2}$ and Sn^{2+} $3d_{3/2,}$ respectively. The binding energy separation between the Sn-3$d_{3/2}$ and Sn-3$d_{5/2}$ levels was found to be 8.51 eV. This result shows the formation of Sn^{2+}.

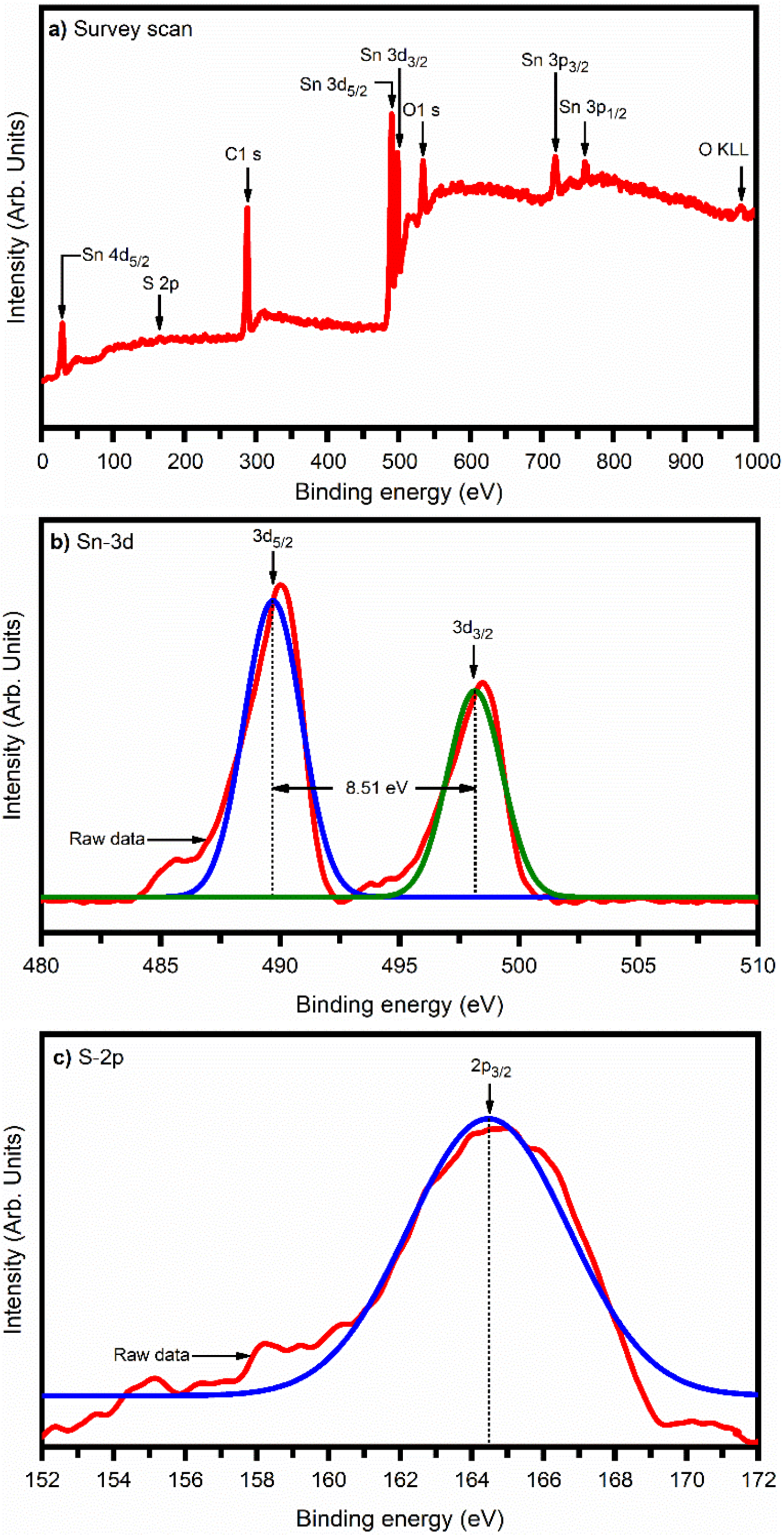

Figure 5: a) XPS spectra for SnS thin film survey scan in the range 0 eV-1000 eV **b)** Sn-3d spectra in the range 480 eV-510 eV **c)** S-2p spectra in the range 152 eV-172 eV**.**

Figure 5(c) shows the S peak at ~ 164.48 eV, which corresponds to the binding energy of S-2$p_{3/2}$ bonded in SnS. These results match the previously available data in the literature [68, 69]. Thus, the XPS results further confirm the formation of pure-phase SnS without the growth of undesired phases or oxidized phases under the prevailing experimental conditions.

3.2: Optical properties

The optical properties such as absorption and band gap of SnS nanoflake film were investigated using UV-Visible-NIR spectroscopy. The absorbance (A) of SnS nanoflake film was calculated using transmittance data obtained from UV-Visible-NIR spectroscopy using,

$$A = -\log(T) = -\log\left(\frac{I_O}{I_t}\right) \qquad \text{..... (5)}$$

Where, T is transmittance, I_O is the radiant power or irradiance, and I_t the irradiance leaving the sample after interacting with it.

Figure 6 shows the optical absorbance spectra of SnS nano-flakes film in the range of 200-1200 nm. It exhibits a sharp absorption edge in the UV region, which indicates that SnS nano-flakes film has a high degree of crystallinity. The XRD analysis support this conjecture. Furthermore, the absorption plot indicates the indirect bandgap nature of the SnS films.

The absorption coefficient (α) was deduced using the absorbance using Beer-Lambert's law,

$$\alpha = 2.303\left(\frac{A}{t}\right) \qquad \text{..... (6)}$$

Where t is the thickness of the thin film.

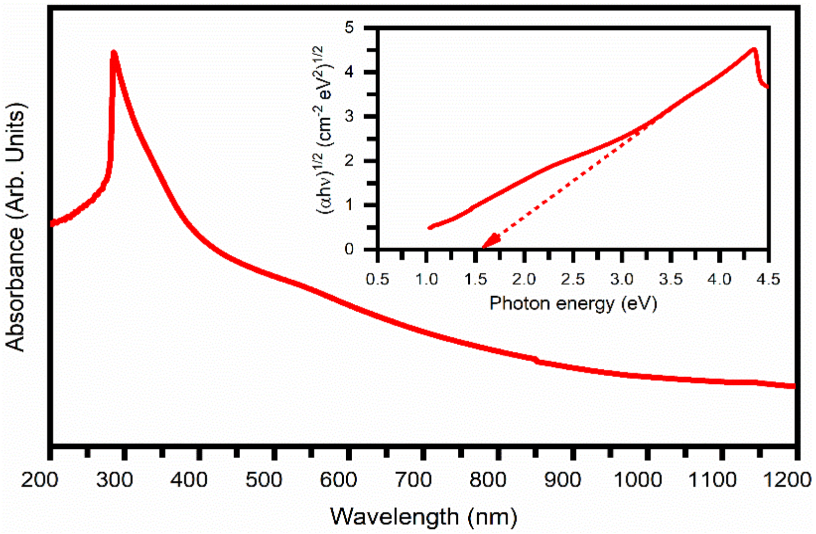

Figure 6: Optical absorption spectra of SnS nano-flakes film. Inset is Tauc's plot for the estimation of the bandgap.

The optical energy band gap (E_{opt}) was determined from the optical absorption data using the near-band edge absorption relation [70],

$$(\alpha h\upsilon)^{n} = B\,(h\upsilon - E_{Opt}) \qquad \text{….. (7)}$$

Where B is a constant known as the band tailing parameter, h is Plank's constant, υ is photon frequency, E_g is the bandgap of the material, and n is the power factor of the transition mode, which is dependent upon the nature of the material. For direct allowed and forbidden transitions, n = 2 and 2/3 respectively, and n = 1/2 and 1/3 for indirect allowed and forbidden transitions. The optical band gap is obtained by extrapolating the tangential line to the photon energy (E = hυ) axis in the plot of $(\alpha h\upsilon)^{1/2}$ as a function of hυ (Tauc plot). The inset of figure 6 shows the typical Tauc plot for SnS nanoflakes. The estimated value of the band gap is found ~ 1.66 eV, which is in close agreement with previous reports [71,72].

3.5: Field emission studies

The field emission (FE) properties of the SnS nanoflakes emitter were measured in a planar diode configuration in an all-metal ultra-high vacuum (UHV) system. The field emission properties of SnS nanoflakes are shown in Figure 7. Figure 7(a) represents the variation of emission current density (J) as a function of an applied electric field (E) of SnS nanoflakes. Before measuring the J-E observations, surface asperities and contaminants were removed by residual gas ion bombardment. For this, the emitter (SnS nanoflakes) was kept at 2 kV with respect to the anode for 5 min. In the present studies, the applied field (E) is defined as E = V/d, where V is the applied voltage and d is the separation between the emitter and the anode (1 mm). The emission current density (J) is estimated as J = I/A, where I is the measured value of emission current, and A is the actual (total) area of the emitter surface (1 cm^2). Figure 7(a) shows the value of the turn-on field, defined as the field required to draw a current emission density of 10 $\mu A/cm^2$, which was found to be ~ 2.5 V/µm for the SnS nanoflakes emitter. Furthermore, the exponential increase in emission current density with a gradual increase in the applied field indicates that the emission is as per the Fowler-Nordheim theory [73]. The maximum emission current density of ~ 104 $\mu A/cm^2$ has been drawn from the emitter at the applied field ~ 8.0 V/µm. A comparison of the reported values of turn-on field for various metal chalcogenide nanostructures emitters with the value obtained in the present study is depicted in Table 1. The low value of the turn-on field can be attributed to the high aspect ratio, smaller areal density, negligible screening effect, and narrow band gap of the SnS nanoflakes [21].

Table 1: A comparison of the reported values of turn-on field for various metal chalcogenide nanostructures emitters

Material	Morphology	Synthesis route	Turn-on field (V/µm)	Reference
CdS	Nanowires	Thermal evaporation	9.0 @ 10 µA/cm2	[74]
Bi_2S_3	Nanoflowers	Vapor deposition	7.45 @ 0.01 mA/cm^2	[75]
CuS	Nanowalls	Vapor-solid phase reaction	8.5 @ 10 µA/cm2	[76]
ZnS	Nanotubes	Carbothermal-CVD	5.43 @ 10 µA/cm2	[77]
GaS	Nanobelts	Thermal evaporation	2.9 @ 0.1 nA/cm2	[78]
SnS	**Nano-flakes**	**Hot injection method**	**6.2** @ 10 µA/cm2	**Present work**

According to *Fowler and Nordheim* [79], the dependence of field emission current density over the applied field is theoretically explained by the equation,

$$J = \lambda_M \, a \, \phi^{-1} \, E^2 \, \beta^2 \exp\left(-\frac{b\phi^{\frac{3}{2}}}{\beta E} \, \nu_F\right) \qquad \text{..... (8)}$$

Where a and b are constants, typically 1.54×10^{-6} A eV/V^2 and 6.83 $eV^{-3/2}$ V/nm, respectively. The ϕ is the work function of the emitter material, λ_M is the macroscopic pre-exponential correction factor, ν_F (correction factor) is the value of principal Schottky-Nordheim barrier function, and β is the field enhancement factor. The observed J-E characteristic is analyzed further by plotting a graph of ln(J/E^2) versus (1/E) known as the Fowler-Nordheim (F-N) plot. Figure 7(b) shows the F-N plot for SnS nanoflakes. As seen, the F-N plot exhibits overall nonlinear behavior over the entire range of the applied field, indicating the semiconducting nature of the SnS nanoflakes. Similar nonlinear F-N plots have been reported for other semiconductors [80, 81]. The field enhancement factor (β) can be calculated from the F-N plot using the relation,

$$\beta = \frac{(6.8\times10^3)\phi^{\frac{3}{2}}}{\text{Slope}} \qquad \text{.....(9)}$$

Where, ϕ is the work function. The estimated value of the enhancement factor is found 1735. Thus, the low value of the work function (4.32 eV) and the high value of β (1735) may be further responsible for improved field emission characteristics of the SnS nanoflakes.

For practical application of SnS nano-flakes as a cold cathode, field emission current stability is a critical parameter. The emission current versus time (I-t) plots corresponding to the preset values of 1 µA, recorded at a base pressure of 10^{-8} mbar with a sampling time of 10 s for more than 2 hrs duration, are shown in figure 7(c). A stable emission current > 1 µA has been observed for more than 2 hrs, which is vital for device fabrication. Some fluctuations/spikes were observed in the I-t plots, which can be attributed to the adsorption/desorption of residual gas molecules over the emitter surface [82].

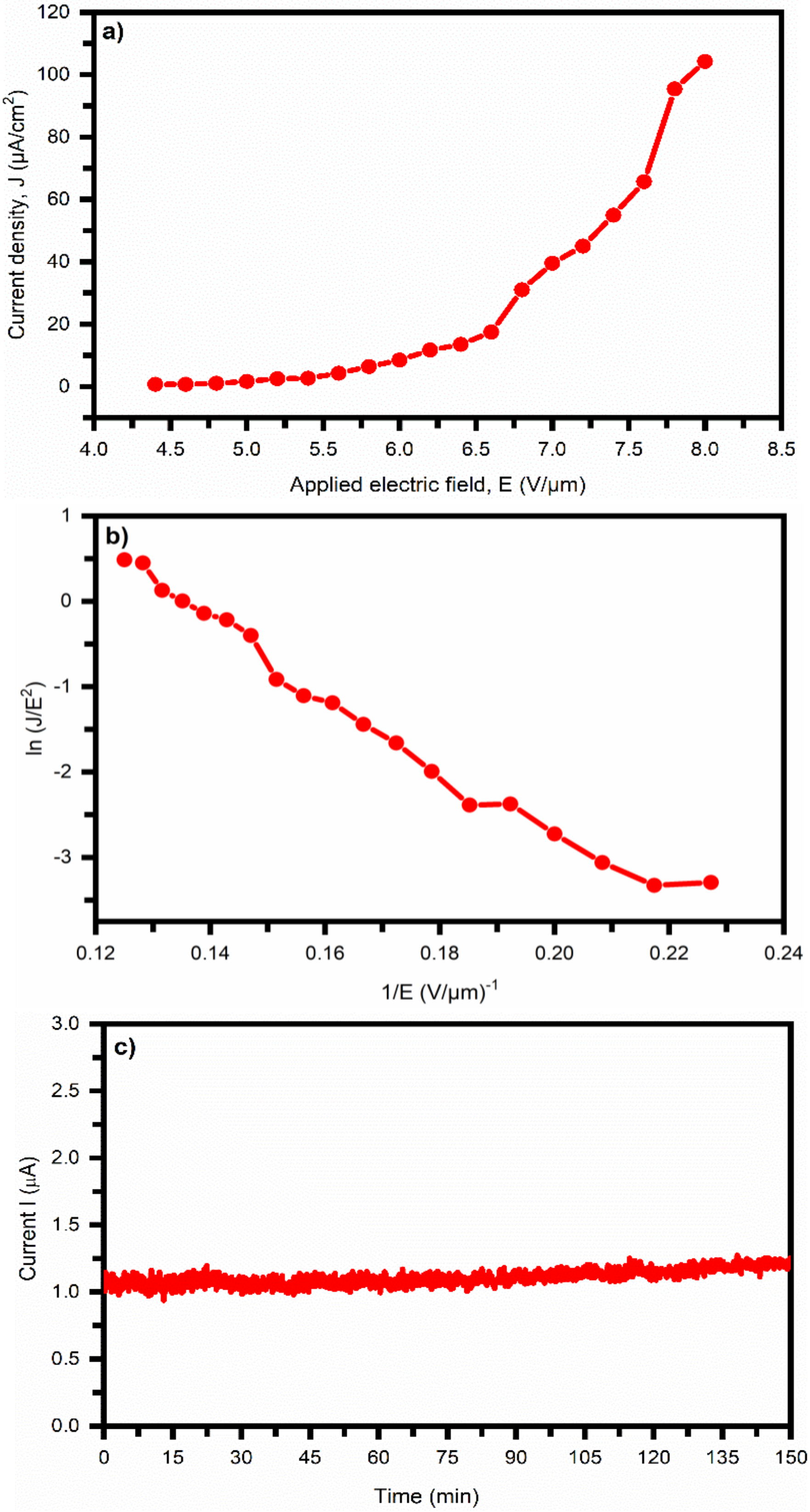

Figure 7: Field emission investigation of SnS nanoflakes using **a)** Applied electrical field as a function of emission current density, **b)** F-N plot showing nonlinear behavior, **c)** Emission current as a function of time (I-t plot).

3.6: Density functional theory (DFT) investigation

Following the experimental results, further specific insight into the field emission properties of SnS can be attained using molecular level DFT calculations. The orthorhombic structure found in the experiment has been used to model SnS [Figure 8(a)] and its properties, finding cell parameters of a = 0.398 nm, b = 0.441 nm, c = 1.129 nm, following our XRD data. The bandgap for SnS was calculated to be 1.48 eV and is shown to be an indirect bandgap from the corresponding band structure [Figure 8(b)], which is in good agreement with the UV-Visible spectroscopy analysis and Tauc plot. Photochemical information can be provided by analyzing the partial density of states (PDOS) [Figure 8(c)], showing the chemical states occupying the valence and conduction levels of the semiconducting material.

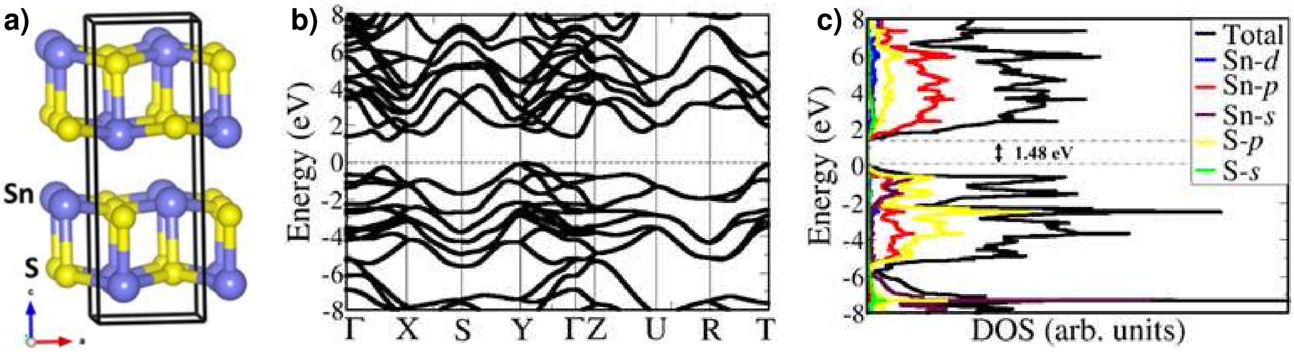

Figure 8: a) The bulk SnS crystal structure, **b)** band structure, and **c)** corresponding projected density of states (PDOS), showing the orbital contributions towards the valence and conduction bands.

The valence band is found to be composed primarily of S-p states with some Sn-d states. Sn-p dominates the conduction band, on the other hand, with smaller contributions from S-p states. The surface energies of the (001), (010), and (111) surfaces [Figure 9(a)-9(c)] are calculated to be 0.26 J/m^2, 0.47 J/m^2, and 0.87 J/m^2, respectively. Consistent with its creation involving only breaking the weak Van der Waals interactions between the SnS layers, the (001) surface [Figure 9(a)] is predicted to be by far the most stable surface. From predicted surface energies, the equilibrium Wulff shape of the SnS nano-flakes was constructed. Due to its relative stability, the (001) facet occupies the largest area of the tabular SnS nanoflakes, whose edges are composed of the (010) and (111) facets. For field emission applications, a lower work function is preferred to enable facile electron emission. The work function of the (001), (010), and (111) surfaces was calculated to be 4.32 eV, 4.67 eV, and 4.64 eV, respectively. Therefore, it shows the (001) surface has the optimal work function to achieve higher field emission characteristics. The DFT investigation for field emission applications has been reported previously [62, 83, 84].

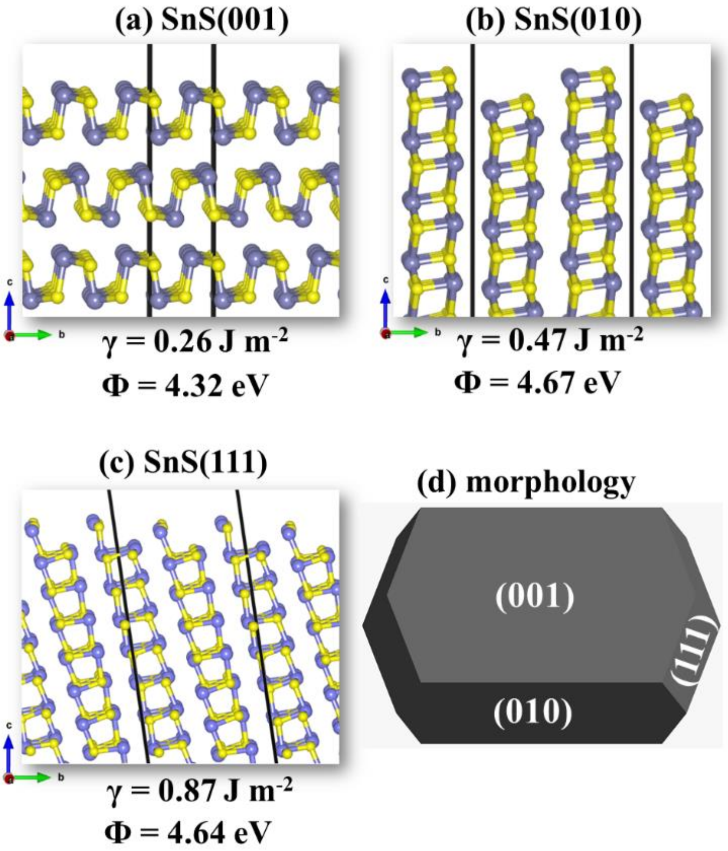

Figure 9: The optimized structures of **a)** (001), **b)** (111), **c)** (010) SnS surfaces with the calculated surface energy (γ) and work function (ϕ) displayed below, and **d)** The equilibrium Wulff construction of the SnS nanocrystal.

4: CONCLUSION

A combination of experimental and computational approaches was employed to characterize and assess the structural, opto-electronic, morphological, and field emission properties of the SnS nanoflakes. SnS nanoflakes were synthesized by a low-cost, non-toxic, and facile hot injection method. The XRD and Raman analysis indicate the formation of polycrystalline orthorhombic SnS nano-structures. The phase-pure and polycrystalline SnS nano-structures confirmed by XRD and Raman analyses exhibit a bandgap of 1.66 eV as estimated from UV-Visible-NIR absorption spectroscopy measurements and validated by first-principles DFT calculations which predicts a bandgap of 1.48 eV. The SnS nanoflakes demonstrate a current density of 10 µA/cm^2 at an applied field of 6.2 V/µm with an enhancement factor of 1735. The predicted lower work function of different surfaces, especially for the most stable SnS (001) surface (ϕ = 4.32 eV) is deemed to be responsible for the observed facile electron emission characteristics. The experimental and theoretical investigations presented in this study successfully interpreted the improved field emission characteristics of SnS nanoflakes.

ACKNOWLEDGMENTS

SRR, RWC and NYD acknowledge the UK Engineering and Physical Sciences Research Council (EPSRC) for funding (Grant No. EP/S001395/1). This work has also used the Advanced Research Computing computational facilities at Cardiff (ARCCA) Division, Cardiff University, and HPC Wales. This work also made use of the facilities of ARCHER (http://www.archer.ac.uk), the UK's national supercomputing service, via the membership of the UK's HEC Materials Chemistry Consortium, which is funded by EPSRC (EP/L000202). YAJ thanks SPPU PDF and School of Energy Studies, SPPU, for financial support and access to laboratory facilities. Sandesh Jadkar is thankful to the Indo-French Centre for the Promotion of Advanced Research-CEFIPRA, Department of Science and Technology, New Delhi for special financial support, and UGC for the financial support UPE program.

CONFLICTS OF INTEREST

There are no conflicts to declare.

REFERENCES:

REFERENCES:

[1] S. Zhuiykov, In Electronic devices and functional structures based on nanostructured semiconductors, Nanostructured Semiconductor Oxides for the Next Generation of Electronics and Functional Devices, Woodhead Publishing, 2014, Pages 95-138.

[2] A. Thapa, Y. Poudel, R. Guo, K. Jungjohann, X. Wang, W. Li, Direct synthesis of micropillars of vertically aligned carbon nanotubes on stainless-steel and their excellent field emission properties, Carbon 171 (2021) 188-200. https://doi.org/10.1016/j.carbon.2020.08.081.

[3] X. Guo, Y. Li, Y. Ding, Q. Chen, J. Li, Direct patterned growth of intrinsic/doped vertical graphene nanosheets on stainless steel via heating solid precursor films for field emission application, Materials & Design, 162 (2019) 293-299. https://doi.org/10.1016/j.matdes.2018.11.056.

[4] A. Pelella, A. Grillo, F. Urban, F. Giubileo, M. Passacantando, E. Pollmann, S. Sleziona, M. Schleberger, A. Bartolomeo, Gate-Controlled Field Emission Current from MoS2 Nanosheets, Advanced Electronic Materials, 7 (2021) 2000838. https://doi.org/10.1002/aelm.202000838.

[5] G. Sinha, S. Panda, A. Datta, P. Chavan, D. Shinde, M. More, D. Joag, A. Patra, Controlled growth of well-aligned GaS nanohornlike structures and their field emission properties, ACS Appl. Mater. Interfaces 3 (2011) 2130-2135. https://doi.org/10.1021/am200339v.

[6] A. Grillo, M. Passacantando, A. Zak, A. Pelella, A. Di Bartolomeo, WS_2 nanotubes: Electrical conduction and field emission under electron irradiation and mechanical stress, Small 16 (2020) 2002880. https://doi.org/10.1002/smll.202002880.

[7] F. Giubileo, E. Faella, A. Pelella, A. Grillo, M. Passacantando, R.Pierre, C. Goosney, A. Bartolomeo, Characterization of InSb nanopillars for field emission applications, Journal of Physics: Conference Series 1765 (2021) 012004. doi:10.1088/1742-6596/1765/1/012004.

[8] D. Late, B. Liu, J. Luo, A. Yan, H. Matte, M. Grayson, C. Rao, V. Dravid, GaS and GaSe ultrathin layer transistors Adv. Mater.24 (2012) 3549-54. DOI: 10.1002/adma.201201361.

[9] Y. Tao, Q. Gao, X. Wang, X. Wu, C. Mao, J. Zhu, NbN and NbS_2 nanobelt arrays: In-situ conversion preparation and field-emission performance, Journal of Nanoscience and Nanotechnology, 11 (2011) 3345-3349. DOI: https://doi.org/10.1166/jnn.2011.3607.

[10] X. Wu, M. Hong, Y. Tao, Y. Deng, Q. Gao, Controlled growth and field-emission properties of $NbSe_2$ micro/nanostructured films, Journal of Nanoscience and Nanotechnology, 10 (2010) 6465-6472. DOI: https://doi.org/10.1166/jnn.2010.2634.

[11] K. Yun, Y. Sun, J. Han, Y. Song, C. Lee, High-performance field-emission properties of boron nitride nanotube field emitters, ACS Appl. Mater. Interfaces 9 (2017) 1562-1568. DOI: 10.1021/acsami.6b10713.

[12] Y. Zhao, Y. Chen, Guofu Zhang, Runze Zhan, Juncong She, Shaozhi Deng, Jun Chen, High current field emission from large-area indium doped ZnO nano-wire field emitter arrays for flat-panel x-ray source application Nanomaterials 11 (2021) 240. ; https://doi.org/10.3390/nano11010240.

[13] S. Suryawanshi, M. More, Exfoliated 2D black phosphorus nanosheets: Field emission studies Journal of Vacuum Science & Technology B 34 (2016) 041803. https://doi.org/10.1116/1.4945433.

[14] X. Wu, Y. Tao, Q. Gao, Preparation and field emission properties of titanium polysulfide nanobelt films, Nano Res. 2 (2009) 558 564. DOI 10.1007/s12274-009-9055-2.

[15] G. Jayalakshmi, K. Saravanan, T. Arun, K. Suresh, B. Sundaravel, B. Panigrahi, D. Kanjilal, Structure and electron field emission properties of ion beam reduced graphene oxide sheets, Carbon 119 (2017) 172-178. https://doi.org/10.1016/j.carbon.2017.04.034.

[16] A. Bhorde, A. Pawbake, P. Sharma, S. Nair, A. Funde, P. Bankar, M. More, S. Jadkar, Solvothermal synthesis of tin sulfide (SnS) nano-rods and investigation of its field emission properties, Applied Physics A 124 (2018) 133. https://doi.org/10.1007/s00339-017-1529-6.

[17] Z. Pan, H. Lai, F. Au, X. Duan, W. Zhou, W. Shi, N. Wang, C. Lee, N. Wong, S. Lee, S. Xie, Oriented silicon carbide nano-wires: Synthesis and field emission properties, Adv. Mater. 16 (2000) 1186-1190. https://doi.org/10.1002/1521-4095.

[18] Y. Xiao, X. Zhang, R. Li, H. Liu, N. Zhou, J. Zhang, Single-crystal LaB6 field emission array is rapidly fabricated by ultraviolet femtosecond laser and its field electronic structure characteristics, Vacuum 184 (2021) 109987. https://doi.org/10.1016/j.vacuum.2020.109987.

[19] Toshiaki Kusunoki, Tomihiro Hashizume, Keigo Kasuya, Noriaki Arai, Stabilization of cold-field-emission current from a CeB6 single-crystal emitter by using a faceted (100) plane, Journal of Vacuum Science & Technology B 39 (2021) 013202. https://doi.org/10.1116/6.0000739.

[20] C. Jadhav, S. Rondiya, R. Hambire, D. Baviskar, A. Deore, R. Cross, N. Dzade, P. Chavan, Highly efficient field emission properties of vertically aligned 2D CuSe nanosheets: An experimental and theoretical investigation, Journal of Alloys and Compounds 875 (2021) 159987. https://doi.org/10.1016/j.jallcom.2021.159987.

[21] S. Suryawanshi, S. Warule, S. Patil, K. Patil, M. More, Vapor-liquid-solid growth of one-dimensional tin sulfide (SnS) nanostructures with promising field emission behavior, ACS Appl. Mater. Interfaces. 6 (2014) 2018–2025. https://doi.org/10.1021/am405039j.

[22] A. Abdelrahman, W. Yunus, A. Arof, Optical properties of tin sulphide (SnS) thin film estimated from transmission spectra, Journal of Non-Crystalline Solids 358 (2012) 1447-1451. doi:10.1016/j.jnoncrysol.2012.03.022.

[23] S. Wang, W. Wang, W. Fong, Y. Yu, C. Surya, Tin Compensation for the SnS Based Optoelectronic Devices, Sci. Rep. 7 (2017) 39704. https://doi.org/10.1038/srep39704.

[24] A. Yago, S. Sasagawa, Y. Akaki, S. Nakamura, H. Oomae, H. Katagiri., H. Araki, Comparison of buffer layers on SnS thin-film solar cells prepared by co-evaporation, Phys. Status Solidi C 14 (2017) 1600194. https://doi.org/10.1002/pssc.201600194.

[25] S. Hortikar, V. Kadam, A. Rathi, C. Jagtap, H. Pathan, I. Mulla, P. Adhyapak, Synthesis and deposition of nanostructured SnS for semiconductor-sensitized solar cell, J. Solid State Chem. 21 (2017) 2707-2712. https://doi.org/10.1007/s10008-017-3642-z.

[26] J. Huang, J. Chen, L. Ma, Q. Liu, M. Wang, L. Liao, T. Rujiralai, L. Xu, In-situ coupling SnS with nitrogen-doped porous carbon for boosting Li-storage in lithium-ion battery and capacitor, Electrochimica Acta, 365 (2021) 137350. https://doi.org/10.1016/j.electacta.2020.137350

[27] M. Mahdi, I. Hmood, N. Ahmed, F. Mustafa, S. Azzez, High performance near infrared photodetector based on cubic crystal structure SnS thin film on a glass substrate, Mater. Lett. 200 (2017) 10-13. https://doi.org/10.1016/j.matlet.2017.04.077.

[28] S. Hegde, B. Surendra, V. Talapatadur, Prashantha Murahari, K.Ramesh, Visible light photocatalytic properties of cubic and orthorhombic SnS nanoparticles, Chemical Physics Letters 754 (2020) 137665. https://doi.org/10.1016/j.cplett.2020.137665.

[29] M. Afsar, M. Rafiq, A. Tok, Two-dimensional SnS nano-flakes: synthesis and application to acetone and alcohol sensors, RSC Adv. 7 (2017) 21556-21566. https://doi.org/10.1039/C7RA03004E.

[30] F. Essa, J. Yu, A. Elsheikh, M. Tawfik, A new M50 matrix composite sintered with a hybrid SnS/ZnO nanoscale solid lubricants: an experimental investigation, Materials Research Express, 6 (2019) 116523. https://doi.org/10.1088/2053-1591/ab4675.

[31] H. Chauhan, M. Singh, S. Hashmi, S. Deka, Synthesis of surfactant-free SnS nano-rods by a solvothermal route with better electrochemical properties towards supercapacitor applications, RSC Adv. 5 (2015) 17228-17235. https://doi.org/10.1039/C4RA15563G.

[32] M. Fenech, N. Sharma, Pulsed laser deposition-based thin film microbatteries, Chemistry-An Asian Journal 15 (2020) 1829-1847. https://doi.org/10.1002/asia.202000384.

[33] K. Manukumar, G. Nagaraju, Brij Kishore, C. Madhu, N. Munichandraiah, Ionic liquid-assisted hydrothermal synthesis of SnS nanoparticles: Electrode materials for lithium batteries, photoluminescence and photocatalytic activities Journal of Energy Chemistry, 27 (2018) 806-812. https://doi.org/10.1016/j.jechem.2017.05.010.

[34] D. Lee, J.Y. Cho, H.S. Yun, D.K. Lee, T. Kim, K. Bang, Y.S. Lee, H.Y. Kim, J. Heo, Vapor transport deposited tin monosulfide for thin-film solar cells: Effect of deposition temperature and duration, J. Mater. Chem. A., 7 (2019) 7186-7193, https://doi.org/10.1039/c8ta09820d.

[35] S. Kabouche, Y. Louafi, B. Bellal, M. Trari, Electrochemical growth of SnS thin film: application to the photocatalytic degradation of rhodamine B under visible light, Applied Physics A 123 (2017) 545. https://doi.org/10.1007/s00339-017-1155-3.

[36] S. Gedi, V. Reddy, M. Reddy, J. Kang, C. Jeon, Impact of high temperature and short period annealing on SnS films deposited by E-beam evaporation, Applied Surface Science 402 (2017) 463-468. https://doi.org/10.1016/j.apsusc.2017.01.113.

[37] J. Jing, M. Cao, C. Wu, J. Huang, J. Lai, Y. Sun, L. Wang, Y. Shen, Chemical bath deposition of SnS nanosheet thin films for FTO/SnS/CdS/Pt photocathode, Journal of Alloys and Compounds 726 (2017) 720-728. https://doi.org/10.1016/j.jallcom.2017.07.303.

[38] N. Wongcharoen, T. Gaewdang, Influence of Annealing Temperature on the Properties of SnS thin films prepared by vacuum thermal evaporation, Materials Science Forum 890 (2017) 295-298. https://doi.org/10.4028/www.scientific.net/MSF.890.295.

[39] L. Cheng, M. Liu, M. Wang, S. Wang, G. Wang, Q. Zhou, Z. Chen, Preparation of SnS films using solid sources deposited by the PECVD method with controllable film characters, Journal of Alloys and Compounds 545 (2012) 122-129. https://doi.org/10.1016/j.jallcom.2012.07.144.

[40] M. Zaman, R. Poolla, S. Khandy, A. Modi, R. Tiwari, Thioglycolic acid assisted hydrothermal growth of SnS 2D nanosheets as catalysts for photodegradation of industrial dyes, Nanotechnology, 32 (2021) 245706. https://doi.org/10.1088/1361-6528/abec09.

[41] T. Sall, B. Soucase, M. Mollar, J. Sans, SnS thin films prepared by chemical spray pyrolysis at different substrate temperatures for photovoltaic applications, Journal of Electronic Materials, 46 (2017) 1714-1719. https://doi.org/10.1007/s11664-016-5215-9.

[42] S. Banu, S. Ahn, Y. Eo, J. Gwak, Ara Cho, Tin monosulfide (SnS) thin films grown by liquid-phase deposition, Solar Energy 145 (2017) 33-41.https://doi.org/10.1016/j.solener.2016.12.013.

[43] A. Catherall, S. Harris, M. Hill, A. Johnson, M. Mahon, Deposition of SnS thin films from Sn(II) thioamidate precursors, Growth Des. 17 (2017), 5544-5551. https://doi.org/10.1021/acs.cgd.7b01100.

[44] S. Chaki, M. Chaudhary, M. Deshpande, SnS thin films deposited by chemical bath deposition, dip coating, and SILAR techniques, J. Semicond. 37 (2016) 053001-9. https://doi.org/10.1088/1674-4926/37/5/053001.

[45] K. Modi, P. Pataniya, V. Patel, C. Sumesh, Microwave assisted synthesis of SnS nanosheets for fabrication of large area SnS/Si heterojunction, Solar Energy 221 (2021) 412-417. https://doi.org/10.1016/j.solener.2021.04.061.

[46] Y. Wu, T. Wei, X. An, L.M. Liu, Colloidal synthesis of SnS nanocrystals with dimension-dependent photoelectrochemical properties, New J. Chem. 43 (2019) 7457–7462. https://doi.org/10.1039/c9nj00506d.

[47] D. Koktysh, J. McBride, R. Geil, B. Schmidt, B. Rogers, S. Rosenthal, Facile route to SnS nanocrystals and their characterization, Materials Science and Engineering B 170 (2010) 117-122. doi:10.1016/j.mseb.2010.03.035.

[48] M. Khan, J. Akhtar, M. Malik, M. Akhtar, N. Revaprasadu, Phase-pure fabrication and shape evolution studies of SnS nanosheets, New J. Chem. 39 (2015) 9569-9574. DOI: 10.1039/C5NJ01919B.

[49] P. Huang, J. Huang, S. Wang, M. Shaikh, C. Line, Photoelectrochemical properties of orthorhombic and metastable phase SnS nanocrystals synthesized by a facile colloidal method, Thin Solid Films, 596 (2015) 135-139. https://doi.org/10.1016/j.tsf.2015.09.081.

[50] C. Tan, H. Zhang, Wet-chemical synthesis and applications of non-layer structured two-dimensional nanomaterials, Nat. Commun. 6 (2015) 7873. https://doi.org/10.1038/ncomms8873.

[51] A. Gupta, T. Sakthivel, S. Seal, Progress in Materials Science Recent development in 2D materials beyond graphene, J. Prog. Mater. Sci. 73 (2015) 44-126. https://doi.org/10.1016/j.pmatsci.2015.02.002.

[52] D. Joubert, From ultrasoft pseudopotentials to the projector augmented-wave method, Phys. Rev. B Condens. Matter Mater. Phys. 59 (1999) 1758-1775. https://doi.org/10.1103/PhysRevB.59.1758.

[53] R. Hernández, Efficient iterative schemes for ab initio total-energy calculations using a plane-wave basis set, J. Phys. Chem. A. 124 (2020) 4053-4061. https://doi.org/10.1021/acs.jpca.0c01375.

[54] J. Perdew, K. Burke, M. Ernzerhof, Generalized gradient approximation made simple, Phys. Rev. Lett. 77 (1996) 3865-3868. https://doi.org/10.1103/PhysRevLett.77.3865.

[55] A. Krukau, O. Vydrov, A. Izmaylov, G. Scuseria, Influence of the exchange screening parameter on the performance of screened hybrid functionals, J. Chem. Phys. 125 (2006). https://doi.org/10.1063/1.2404663.

[56] K. Hu, M. Wu, S. Hinokuma, T. Ohto, M. Wakisaka, J. Fujita, Y. Ito, Special points for Brillonin-zone integrations, J. Mater. Chem. A. 7 (2019) 2156-2164. https://doi.org/10.1039/c8ta11250a.

[57] P. Blöchl, O. Jepsen, O. Andersen, Improved tetrahedron method far Brilleuin-zane integratians, Phys. Rev. B. 49 (1994) 16223-16233.

[58] G. Watson, E. Kelsey, N.Leeuw, D. Harris, S. Parker, Atomistic simulation of dislocations, surfaces and interfaces in MgO, J. Chem. Soc.-Faraday Trans. 92 (1996) 433-438. https://doi.org/10.1039/ft9969200433.

[59] P. Tasker, The stability of ionic crystal surfaces, J. Phys. C Solid State Phys. 12 (1979) 4977-4984. https://doi.org/10.1088/0022-3719/12/22/036.

[60] N. Dzade, N. Leeuw, Periodic DFT+U investigation of the bulk and surface properties of marcasite (FeS2), Phys. Chem. Chem. Phys. 19 (2017) 27478–27488. https://doi.org/10.1039/C7CP04413E.

[61] P. Baviskar, S. Rondiya, G. Patil, B. Sankapal, H. Pathan, P. Chavan, N. Dzade, ZnO/CuSCN Nano-Heterostructure as a Highly Efficient Field Emitter: A Combined Experimental and Theoretical Investigation, ACS Omega. 5 (2020) 6715-6724. https://doi.org/10.1021/acsomega.0c00006.

[62] N. Reddy, M. Devika, E. Gopal, Review on Tin (II) Sulfide (SnS) Material: Synthesis, Properties, and Applications, Crit. Rev. Solid State Mater. Sci. 40 (2015) 359–398. https://doi.org/10.1080/10408436.2015.1053601.

[63] J. Chao, Z. Xie, X. Duan, Y. Dong, Z. Wang, J. Xu, B. Liang, B. Shan, J. Ye, D. Chen, G. Shen, Visible-light-driven photocatalytic and photoelectrochemical properties of porous SnSx (x = 1, 2) architectures, CrystEngComm. 14 (2012) 3163-3168. https://doi.org/10.1039/c2ce06586j.

[64] B. Cullity, S. Stock, Elements of X-ray Diffraction, 3rd Edn., Princeton Hall, New York, 2001

[65] H. Kafashan, Structural characterizations of pure SnS and In-doped SnS thin films using isotropic and anisotropic models, Mater. Res. Express. 5 (2018). https://doi.org/10.1088/2053-1591/aabdb8.

[66] M. Takahashi, Half-filled Hubbard model at low temperature, J. Phys. C Solid State Phys. 10 (1977) 1289-1301. https://doi.org/10.1088/0022-3719/10/8/031.

[67] M. Patel, A. Chavda, I. Mukhopadhyay, J. Kim, A. Ray, Nanostructured SnS with inherent anisotropic optical properties for high photoactivity, Nanoscale. 8 (2016) 2293-2303. https://doi.org/10.1039/c5nr06731f.

[68] A. Rauf, M.S. Arif Sher Shah, J.Y. Lee, C.H. Chung, J.W. Bae, P.J. Yoo, Non-stoichiometric SnS microspheres with highly enhanced photoreduction efficiency for Cr(VI) ions, RSC Adv. 7 (2017) 30533–30541. https://doi.org/10.1039/c7ra03854b.

[69] X. Guo, H. Xie, J. Zheng, H. Xu, Q. Wang, Y. Li, S. Lee, J. Tang, The synthesis of multi-structured SnS nanocrystals toward enhanced performance for photovoltaic devices, Nanoscale, 7 (2015) 867-871. DOI: 10.1039/c4nr04933k.

[70] J. Tauc, Absorption edge and internal electric fields in amorphous semiconductors, Mater. Res. Bull. 5 (1970) 721-729. https://doi.org/10.1016/0025-5408(70)90112-1.

[71] J. Brent, D. Lewis, T. Lorenz, E. Lewis, N. Savjani, S. Haigh, G. Seifert, B. Derby, P. O'Brien, Tin(II) Sulfide (SnS) Nanosheets by Liquid-Phase Exfoliation of Herzenbergite: IV-VI Main Group Two-Dimensional Atomic Crystals, J. Am. Chem. Soc. 137 (2015) 12689-12696. https://doi.org/10.1021/jacs.5b08236.

[72] C. Yang, Ph. D. Thesis, Harvard University, Cambridge, Massachusetts (2017).

[73] R. Forbes, Field emission: New theory for the derivation of emission area from a Fowler-Nordheim plot, J. Vac. Sci. Technol., B 17 (1999) 526-533. https://doi.org/10.1116/1.590588.

[74] G. Li, Y. Jiang, Y. Zhang, X. Lan, T. Zhai, G.C. Yi, High-performance photodetectors and enhanced field-emission of CdS nanowire arrays on CdSe single-crystalline sheets, J. Mater. Chem. C. 2 (2014) 8252–8258. https://doi.org/10.1039/c4tc01503g.

[75] X. Yu, C. Cao, Photoresponse and field-emission properties of bismuth sulfide nanoflowers, Cryst. Growth Des. 8 (2008) 3951–3955. https://doi.org/10.1021/cg701001m.

[76] X. Feng, Y. Li, H. Liu, Y. Li, S. Cui, N. Wang, L. Jiang, X. Liu, M. Yuan, Controlled growth and field emission properties of CuS nanowalls, Nanotechnology. 18 (2007) 145706. https://doi.org/10.1088/0957-4484/18/14/145706.

[77] U. Gautam, X. Fang, Y. Bando, J. Zhan, D. Golberg, Synthesis, structure, and multiply enhanced field-emission properties of branched ZnS nanotube in nanowire core shell heterostructures, ACS Nano 2 (2008) 1015-1021. https://doi.org/10.1021/nn800013b.

[78] S. Panda, A. Datta, G. Sinha, S. Chaudhuri, P. Chavan, S. Patil, M. More, D. Joag, Synthesis of Well-Crystalline GaS Nanobelts and Their Unique Field Emission Behavior, J. Phys. Chem. C 112 (2008) 6240-6244. https://doi.org/10.1021/jp712083d.

[79] R. Fowler, L. Nordheim, Electron emission in intense electric fields, Proc. R. Soc. London A 119 (1928) 173-181. https://doi.org/10.1098/rspa.1928.0091.

[80] P. Chavan, R. Kashid, S. Badhade, I. Mulla, M. More, D. Joag, CdS nanowires: Ultra-long growth and enhanced field emission properties, Vacuum. 101 (2014) 38-45. https://doi.org/10.1016/j.vacuum.2013.07.019.

[81] S. Rondiya, C. Jadhav, P. Chavan, N. Dzade, Enhanced Field Emission Properties of Au/SnSe Nano-heterostructure: A Combined Experimental and Theoretical Investigation, Sci. Rep. 10 (2020) 1-10. https://doi.org/10.1038/s41598-020-58840-8.

[82] C. Jadhav, B. Pandit, S. Karade, B. Sankapal, P. Chavan, Enhanced field emission properties of V_2O_5/MWCNTs nanocomposite, Appl. Phys. A Mater. Sci. Process. 124 (2018) 1-8. https://doi.org/10.1007/s00339-018-2218-9.

[83] G. Patil, S. Rondiya, V. Bagal, S. Shivhare, R. Cross, N. Dzade, S. Jadkar, P. Chavan, Field Emission Characteristics of Double Walled TiO2 Nanotubes, ES Mater. Manuf. 13 (2021). https://doi.org/10.30919/esmm5f1143.

[84] B. Bade, S. Rondiya, S. Bhopale, N. Dzade, M. Kamble, A. Rokade, M. Nasane, M. More, S. Jadkar, A. Funde, Investigation of growth mechanism for highly oriented TiO2 nanorods: the role of reaction time and annealing temperature, SN Appl. Sci. 1 (2019). https://doi.org/10.1007/s42452-019-09782.